Title
Catalyst electro-redeposition controls morphology and oxidation state for selective carbon dioxide reduction

Journal
Nature Catalysis, 1(2)

ISSN
2520-1158

Authors
De Luna, Phil
Quintero-Bermudez, Rafael
Dinh, Cao-Thang
et al.

Publication Date
2018-02-01

DOI
10.1038/s41929-017-0018-9

Peer reviewed

nature catalysis

ARTICLES

https://doi.org/10.1038/s41929-017-0018-9

Catalyst electro-redeposition controls morphology and oxidation state for selective carbon dioxide reduction

Phil De Luna[1,2,3], Rafael Quintero-Bermudez[4], Cao-Thang Dinh[4], Michael B. Ross[2,3], Oleksandr S. Bushuyev[4], Petar Todorović[4], Tom Regier[5], Shana O. Kelley[6,7], Peidong Yang[2,3,8,9,10,11] and Edward H. Sargent[2,4]*

The reduction of carbon dioxide to renewable fuels and feedstocks offers opportunities for large-scale, long-term energy storage. The synthesis of efficient CO_2 reduction electrocatalysts with high C2:C1 selectivity remains a field of intense interest. Here we present electro-redeposition, the dissolution and redeposition of copper from a sol–gel, to enhance copper catalysts in terms of their morphology, oxidation state and consequent performance. We utilized in situ soft X-ray absorption spectroscopy to track the oxidation state of copper under CO_2 reduction conditions with time resolution. The sol–gel material slows the electrochemical reduction of copper, enabling control over nanoscale morphology and the stabilization of Cu^+ at negative potentials. CO_2 reduction experiments, in situ X-ray spectroscopy and density functional theory simulations revealed the beneficial interplay between sharp morphologies and Cu^+ oxidation state. The catalyst exhibits a partial ethylene current density of 160 mA cm^{-2} (−1.0 V versus reversible hydrogen electrode) and an ethylene/methane ratio of 200.

As energy demand continues to increase, so too do anthropogenic carbon emissions and global temperatures. Renewable energy sources such as solar, wind and hydroelectricity displace fossil fuel carbon emissions and continue to progress to wider deployment. However, long-term (seasonal) energy storage remains a challenge that must be addressed for renewables to meet a major fraction of global energy demand[1]. Carbon dioxide electroreduction to renewable fuels and feedstocks provides an energy storage solution to the seasonal variability of renewable energy sources[2]. When coupled with carbon capture technology, the carbon dioxide reduction reaction (CO_2RR) offers a means to close the carbon cycle.

CO_2RR electrocatalysts lower energetic barriers to CO_2 reduction by stabilizing intermediates and transition states in the multistep electrochemical reduction process[3]. Copper reduces CO_2 to a wide range of hydrocarbon products such as methane, ethylene, ethanol and propanol[4]. Unfortunately, bulk copper is not selective among various carbon products, and it also suffers Faradaic efficiency (FE) losses to the competing hydrogen evolution reaction.

Among possible products, C2+ hydrocarbons are highly sought in view of their commercial value. Ethylene, for example, is a precursor to the production of polyethylene, a major plastic. Selectively producing ethylene over methane circumvents costly paraffin–olefin separation[5]. Developing catalysts that work at ambient conditions to produce C2 selectively over C1 gaseous products will increase the relevance of renewable feedstocks in the chemical sector.

Oxide-derived copper is one class of catalyst that has shown enhanced CO_2RR activity and increased selectivity towards multi-carbon products[6–8]. The selectivity of these catalysts is dependent on structural morphology and copper oxidation state[9–17]. Electrochemical reduction of copper oxide catalyst films can lead to grain boundaries, undercoordinated sites and roughened surfaces that are hypothesized to be catalytically active sites[8,18]. Residual oxides, proposed to play a key role in catalysis, may exist after electrochemical reduction[7]. A recent report of oxygen plasma-activated oxide-derived copper catalysts achieved an ethylene FE of 60% at −0.9 V versus reversible hydrogen electrode (RHE)[9], with activity attributed to the presence of Cu^+ species. In situ hard X-ray absorption spectroscopy (hXAS) experiments have suggested stable Cu^+ species exist at highly negative CO_2RR potentials of ~−1.0 versus RHE[9]. However, the presence of Cu^+ species during CO_2RR is still the subject of debate;[7,19] and in situ tracking of the copper oxidation state with time resolution during CO_2RR has remained elusive.

Morphological effects of copper nanostructures have a significant effect on the selectivity of CO_2RR to multi-carbon products[20–24]. Copper catalysts with different morphologies have been synthesized through annealing, chemical treatments on thin films, colloidal synthesis and electrodeposition from solution[6,17,25,26]. For example, recent work reported selective ethylene production on bromide-promoted copper dendrites with a maximum ethylene FE of 57% (ref. [26]). The selectivity of this catalyst was attributed to the high-index facets and undercoordinated sites on the high-curvature

[1]Department of Materials Science and Engineering, University of Toronto, Toronto, ON, Canada. [2]Bio-inspired Solar Energy Program, Canadian Institute for Advanced Research, Toronto, ON, Canada. [3]Department of Chemistry, University of California, Berkeley, Berkeley, CA, USA. [4]Department of Electrical and Computer Engineering, University of Toronto, Toronto, ON, Canada. [5]Canadian Light Source Inc. (CLSI), Saskatoon, SK, Canada. [6]Department of Pharmaceutical Sciences, Leslie Dan Faculty of Pharmacy, University of Toronto, Toronto, ON, Canada. [7]Department of Biochemistry, Faculty of Medicine, University of Toronto, Toronto, ON, Canada. [8]Department of Materials Science and Engineering, University of California, Berkeley, Berkeley, CA, USA. [9]Materials Sciences Division, Lawrence Berkeley National Laboratory, Berkeley, CA, USA. [10]Chemical Sciences Division, Lawrence Berkeley National Laboratory, Berkeley, CA, USA. [11]Kavli Energy Nanosciences Institute, University of California, Berkeley, Berkeley, CA, USA. Phil De Luna and Rafael Quintero-Bermudez contributed equally to this work. *e-mail: ted.sargent@utoronto.ca

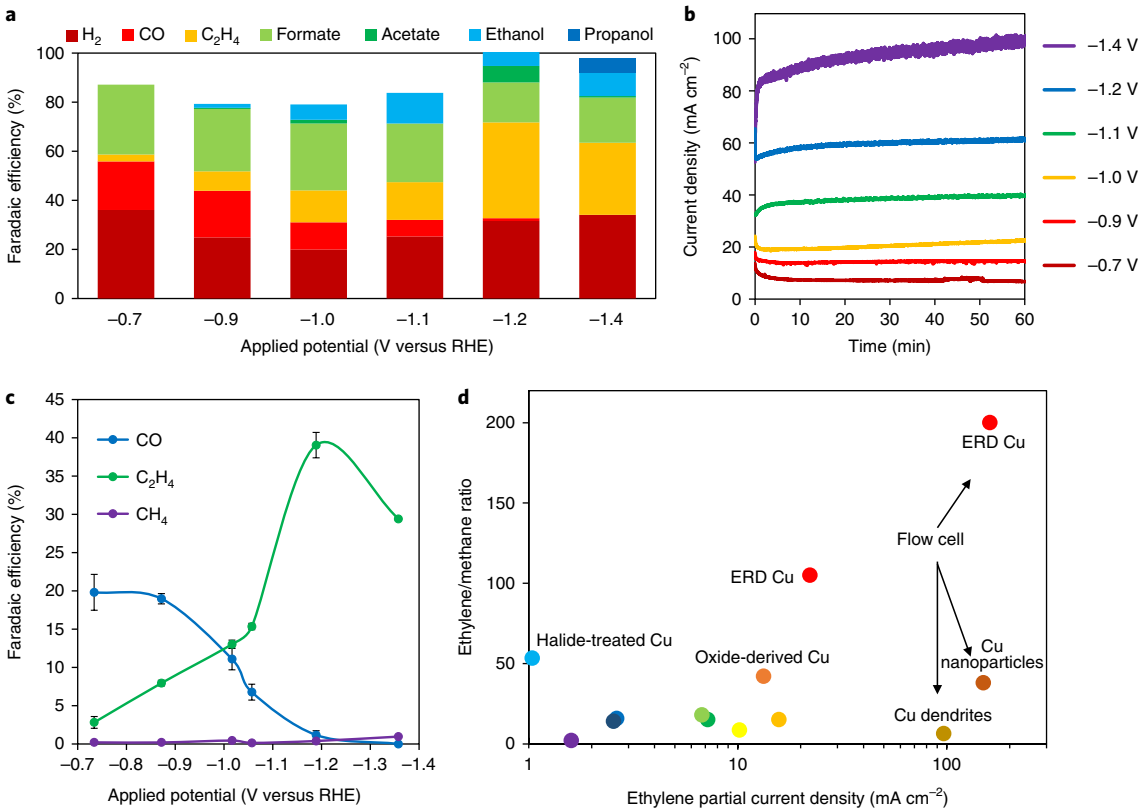

Fig. 1 | Catalytic activity of ERD Cu catalysts. a, FEs of ERD Cu at a range of applied potentials showing all products. **b**, Current densities of the catalyst over 1 h of operation at different applied potentials. **c**, CO_2RR gas product FEs. **d**, Plot of ethylene/methane ratio versus ethylene partial current density for a range of catalysts (for further details, see Supplementary Table 1).

structures[26]. Furthermore, high-curvature structures, such as nanoneedles, promote nucleation of smaller gas bubbles[27], and benefit from field-induced reagent concentration[28–32], where high local negative electric fields concentrate positively charged cations to help stabilize CO_2 reduction intermediates[33], enhancing CO_2RR. However, combining high-curvature morphology with Cu^+ promotion to enable selective chemical conversion has yet to be explored.

Here we report the electro-redeposition of copper from a sol–gel precursor. This process enables simultaneous control over morphology and oxidation state. Time-resolved tracking of the copper oxidation state under in situ CO_2 reduction conditions showed the presence of Cu^+ at highly negative potentials (less than −1.0 V versus RHE). Electro-redeposition exhibits simultaneous in situ dissolution and redeposition of copper from a sol–gel copper oxychloride, enabling a broad range of nanostructures of varying sharpness to be grown from within the bulk material itself. By using in situ soft X-ray absorption (sXAS) spectroscopy, we tracked over time the reduction of copper, revealing the ratio of copper species under different applied potentials. We find the transition from Cu^{2+} to Cu^+ occurs rapidly (within 5 min) whereas the Cu^+ to Cu^0 transition is much slower. Surprisingly, 23% of the catalyst existed as Cu^+ species under a negative applied bias as low as −1.2 V versus RHE for over an hour of operation. The copper oxychloride sol–gel slowed the reduction kinetics of copper, stabilizing Cu^+ at more negative applied potentials. At −1.2 V versus RHE, the electro-redeposited (ERD) copper catalyst exhibited a FE of 54% for C2+ products (ethylene, acetate, ethanol) compared with a FE of 18% for C1 products (carbon monoxide, methane, formate). ERD copper displayed a high ethylene partial current density, within H-cell (22 mA cm^{-2} at −1.2 V versus RHE) and flow-cell (161 mA cm^{-2} at −1.0 V versus RHE) configurations with significant methane suppression and a high ethylene/methane ratio of 200. Density functional theory (DFT) calculations revealed that the formation energy of the ethylene intermediate (OCCOH*) is substantially lowered compared with the methane intermediate (COH*) on a high-curvature surface with Cu^+ species. The in situ XAS and DFT studies, taken together, portray a catalyst in which stabilization of Cu^+ improves selectivity and high-curvature morphology improves activity of C2 production.

Results

Synthesis and CO_2RR activity of ERD Cu. We synthesized the sol–gel copper oxychloride ($Cu_2(OH)_3Cl$) precursor using an epoxide gelation approach to yield a polycrystalline porous material with amorphous regions[34,35]. Scanning electron microscopy (SEM) micrographs of the surface of $Cu_2(OH)_3Cl$ deposited on carbon paper revealed aggregated clusters with 10 nm pores and micrometre void spaces consistent with previous sol–gel reports (Supplementary Fig. 1)[35]. To form the active catalyst, a constant potential was applied in the presence of CO_2-saturated 0.1 M $KHCO_3$ electrolyte to reduce $Cu_2(OH)_3Cl$.

During CO_2RR, the FE_{H2} was found to range from 20 to 36% depending on applied potential (Fig. 1a). The total FE_{CO2RR} was steady at 70% ± 5%. However, the product distribution changed: the major CO_2RR products were C1 products (CO and formate) at lower potentials; and C2+ products (ethylene, acetate and ethanol) at higher negative potentials. The current densities ranged from 10 to 90 mA cm^{-2} depending on applied potential (Fig. 1b). The optimal potential for C2+ products (ethylene, acetate, ethanol and propanol) was −1.2 V versus RHE (Supplementary Fig. 2) with a peak FE of 52% and C2+ partial current density of 31 mA cm^{-2}. The FE_{CO} starts at 20% at −0.7 V versus RHE and decreases to <1% at −1.4 V

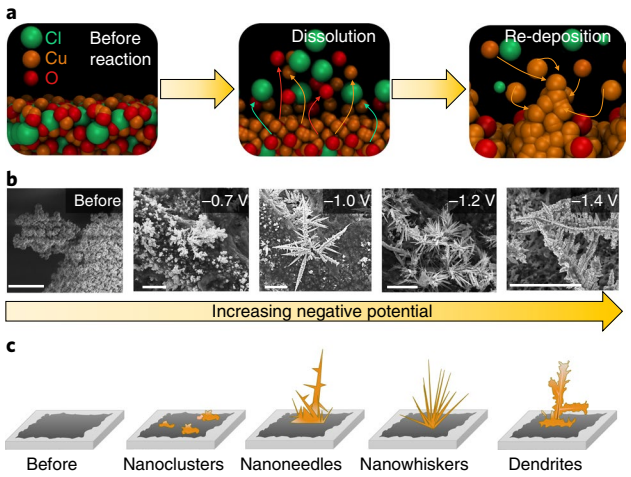

Fig. 2 | Growth of ERD Cu nanostructures. a, Schematic of the electrogrowth process, whereby simultaneous dissolution and redeposition of Cu results in structured deposits. **b**, SEM images of the key structure features at their specific applied potentials after at least 1 h of reaction. Scale bars are 5 µm. **c**, Evolution of nanoclusters (−0.7 V), nanoneedles (−1.0 V), nanowhiskers (−1.2 V) and dendrites (−1.4 V) at increasing negative potential. All potentials are IR corrected and versus RHE.

versus RHE concomitant with an increase in FE_{C2H4} (Fig. 1c). The maximum FE_{C2H4} was 38%. It was found that ERD Cu consistently supresses FE_{CH4} to below 1%.

Structural characterization. We then sought to increase the absolute production of ethylene using a gas flow-cell electrolyser. Increased CO_2 gas diffusion in these configurations have resulted in absolute partial ethylene current densities as high as 150 mA cm^{-2} (refs [26,36]). A maximum FE_{C2H4} of 36% at an ethylene partial current of 161 mA cm^{-2} at −1.0 V versus RHE was observed with extremely strong methane suppression (FE_{CH4} < 0.2%) (Supplementary Fig. 3). A plot of ethylene/methane ratio versus partial current density of ethylene (Fig. 1d), representative of both selectivity and activity, of various Cu catalysts shows ERD Cu exhibits a partial ethylene current density in H-cell and flow-cell systems of 22 mA cm^{-2} and 161 mA cm^{-2}, respectively, with a ethylene/methane ratio of 200.

To understand the formation of the catalyst structure, we carried out SEM, dark-field optical microscopy, transmission electron microscopy (TEM), X-ray diffraction (XRD) and scanning Auger microscopy (SAM) experiments to study ERD Cu over the course of reaction. Depending on the applied potential, different structural morphologies emerged. This growth is due to the simultaneous dissolution and redeposition of Cu ions from the bulk of the material (Fig. 2a). At −0.7 V versus RHE, rounded nanostructures of approximately 0.5 to 5 µm in size formed on the surface (Fig. 2b,c). At −1.0 V versus RHE, sharper needles approximately 5 to 10 µm in length formed. At the more negative potential of −1.2 V versus RHE, sharper nanowhiskers of ~5 to 10 µm with high length-to-diameter ratios were dominant. Finally, at the highest applied potential of −1.4 V versus RHE, dendrites with rounded tips appeared. SEM images were taken after the course of at least 1 h of reduction. The structural features were homogeneously dispersed on the surface of the carbon paper substrate (Supplementary Fig. 4).

Dark field microscope images of blue $Cu_2(OH)_3Cl$ as deposited on carbon paper showed uniform coverage (Supplementary Fig. 5a). Images taken after 1 h of reaction at −0.7 V versus RHE and −1.2 V versus RHE (Fig. 3a,b) show that regions of metallic Cu form on the electrode edges. Microscope images taken of the ERD Cu at −1.4 V versus RHE show the surface dominated by metallic Cu (Supplementary Fig. 5b). TEM images of the catalyst before and after reaction (Fig. 3c,d) reveal the change in the morphology of the material. Before reaction, regions of both polycrystalline and porous disordered material are present in the sol–gel, but after reaction only reduced polycrystalline material remains. XRD spectra were taken of the ERD Cu before and after reaction (Fig. 3e). The precursor sol–gel was found to have some amorphous regions with broad peaks that correspond primarily to $Cu_2(OH)_3Cl$ (ref. [35]). At an applied potential of −0.7 V versus RHE all peaks associated with the precursor have disappeared but notably there are peaks corresponding to Cu_2O and metallic Cu. At more negative potentials, the peaks corresponding to Cu begin to increase while the Cu_2O peak disappears. Using Scherrer's equation[37], we calculated the crystallite sizes to be approximately 18, 25 and 57 nm, for the $Cu_2(OH)_3Cl$ {004} (ref. [38]), Cu_2O {111} (ref. [39]) and Cu {111} (ref. [40]) phases, respectively (Supplementary Table 2), indicating that the crystal grain size increased with applied negative potential. Additional SEM images were taken at 2, 5, 20 and 40 min of Cu electro-redeposition to study the onset growth of sharp nanostructures at −1.0 V versus RHE (Fig. 3f). At 2 min, needle morphologies had begun to form in the sol–gel matrix (Supplementary Fig. 6) and continued to increase in size with respect to time. By 20 min, the needles were fully formed. SAM analysis was performed to determine that the elemental composition of the nanostructures consisted of primarily Cu (Fig. 3g). A line survey scan (Supplementary Fig. 7) showed the presence of Cu and oxygen in the region that the needles grow from. While we cannot exclude the effects of re-oxidation in air, XRD and SAM results, taken together, reveal the morphological evolution of ERD Cu under applied negative potential.

In situ X-ray spectroscopy and surface characterization. The structural evidence for Cu^+ prompted us to investigate further the electronic structure of the catalyst during CO_2RR. We performed in situ sXAS experiments on ERD Cu under CO_2 reduction conditions. Previously, in situ hXAS experiments measuring the metal K-edge were reported for CO_2RR catalysis[9,19,41]. hXAS measurements at the Cu K-edge probe high-energy (9 keV) transitions but do not provide a robust determination of the narrow-band transition metal 3*d* electronic structure because direct excitation of Cu 1*s* electrons into 3*d* orbitals are dipole forbidden. In contrast, sXAS directly measures the dipole-allowed, low-energy (0.93 keV) excitation of a metal 2*p* electron to the partially filled 3*d* shell. Thus, lower-energy transitions can be measured with higher spectral resolution, allowing for the acquisition of more feature-rich spectra that show greater contrast with electronic structure changes.

Ex situ sXAS Cu L-edge measurements of reference standards Cu metal, Cu_2O and CuO were taken (Fig. 4a and Supplementary Fig. 8). These spectra match well in both peak position and line shape with previously published reports[42,43]. The Cu L-edge spectra of the $Cu_2(OH)_3Cl$ precursor at open-circuit potential shows an L_3-edge peak at 930.7 eV and an L_2-edge peak at 950.7 eV, which matches well with CuO, clearly indicating that Cu begins in the +2 oxidation state (Supplementary Fig. 9). We began by applying a constant potential of 1.13 V versus RHE and measuring the Cu L-edge over the course of 5 min (5 scans × 1 min each) under CO_2RR conditions. We then applied a more negative constant potential and re-measured the Cu L-edge for another 5 min continuing in a step-wise fashion up to −1.87 V versus RHE.

The evolution of the Cu L_3-edge as a function of potential was tracked (Fig. 4a). We found that at applied potentials more positive than 0.28 V versus RHE, the Cu L-edge exhibits a distinct peak at 931 eV, which is consistent with Cu^{2+} (ref. [43]). At 0.28 V versus RHE, we observed that the sXAS spectra changed rapidly between each 1 min scan (Fig. 4b). We tracked, in real-time, the transition of Cu from Cu^{2+} to Cu^+ as the L_3-edge peak associated with Cu^{2+} at 931 eV decreased while another higher-energy peak around

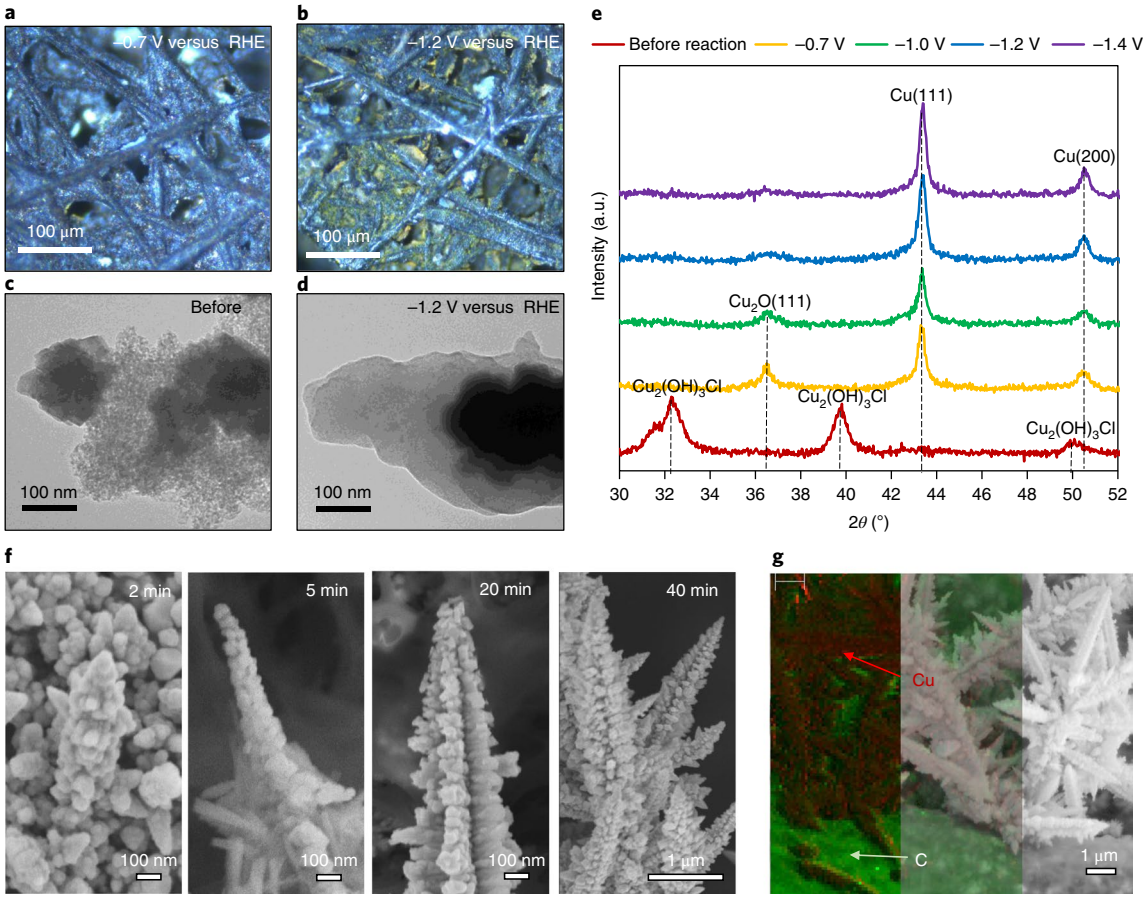

Fig. 3 | Surface characterization of ERD Cu. a,**b**, Dark-field microscope images of ERD Cu after 1 h of reaction at −0.7 V versus RHE (**a**) and −1.2 V versus RHE (**b**). **c**,**d**, TEM images of ERD Cu before reaction (**c**) and after (**d**) reaction. **e**, XRD plot of the ERD Cu before reaction (red) and after reaction at varying applied potentials. **f**, SEM images of ERD Cu under −1.0 V versus RHE taken at 2, 5, 20 and 40 min from left to right. **g**, SAM images of ERD Cu showing the Cu nanostructures (red) on carbon (green).

934 eV began to emerge, consistent with an L_3-edge peak of 933.7 eV for Cu_2O (ref. [43]). By observing the change in sXAS spectra with respect to time, we found the structural change of Cu from Cu^{2+} to Cu^+ occurred rapidly within 5 min. At applied potentials more negative than 0.28 V versus RHE, we continued to observe a prominent sharp peak at 933 eV, which is consistent with Cu^+. As the potentials approached reducing conditions lower than 0 V versus RHE, the high-energy intensity past the adsorption L_3-edge increased, characteristic of bulk Cu, and can be explained by transitions into 4*s* states unhybridized with 3*d* states[43]. Finally, at the applied potential of −1.87 V versus RHE, we found that the spectrum matched bulk Cu, indicating a complete transition from Cu^+ to Cu^0. There was little variation between scans of the same applied potential, indicating the transition from Cu^+ to Cu^0 was not as rapid as the Cu^{2+} to Cu^+ transition.

To provide a more quantitative analysis of the oxidation state changes during CO_2RR, we fitted the in situ spectra with a linear combination of the Cu metal, Cu_2O and CuO standards. A linear combination of the sXAS spectra was fitted to the Cu L_3-edge spectra taken at 0.43 V, 0.13 V and −1.87 V versus RHE (Supplementary Fig. 10 and R^2 values in Supplementary Table 3). From the linear combination, we calculated the ratio of Cu oxidation species present at each applied potential (Fig. 4d), assuming the reference measurements provide an accurate representation of the 0, +1 and +2 oxidation states. Remarkably, we found that Cu(I) existed even at the negative potential of −1.47 V versus RHE under CO_2RR conditions.

We tracked the change, over time and under applied bias (required for ethylene production (−1.2 V versus RHE), to determine the Cu species present during reaction (Fig. 4c). After 2 min, the majority of Cu (84%) was in the Cu^+ oxidation state (Fig. 4e). After a further 10 min, this had decreased to 77%. The decrease of 7% of Cu^+ over 10 min is consistent with the potential-dependent in situ data, which reveal that the transition between Cu^{2+} and Cu^+ is a rapid one, while the transition between Cu^+ and Cu^0 is much slower. After 1 h under applied potential of −1.2 V versus RHE, 23% of Cu^+ remained. In situ hXAS experiments also showed a more oxidized Cu species on ERD Cu after 1 h of operation compared with Cu foil (Supplementary Fig. 11). These results show that Cu^+ may be stabilized under an applied potential of −1.2 V versus RHE for over 1 h.

Two-dimensional contour maps of the Cu $L_{\alpha,\beta}$ fluorescence intensity (Fig. 4f,g) revealed that the Cu signal is dispersed throughout the sample area before reaction. After reduction, localized regions of higher intensity appear; suggesting Cu aggregation. Because halides are known to impact CO_2RR, X-ray photoelectron spectropscopy (XPS) was performed to study the presence of chlorine on the surface of the catalyst. XPS results (Supplementary Fig. 12) showed that no chlorine remained on the surface of the sample after reaction. Furthermore, the oxygen intensity also decreased substantially after reaction, indicating the reduction of CuO. The change in the Cu 2*p* peak is most indicative of reaction: before reaction, a sharp chemical shift is observed typical of a copper hydroxide species like $Cu_2(OH)_3Cl$[44], while after reaction, the Cu $2p_{3/2}$ exhibits a signature

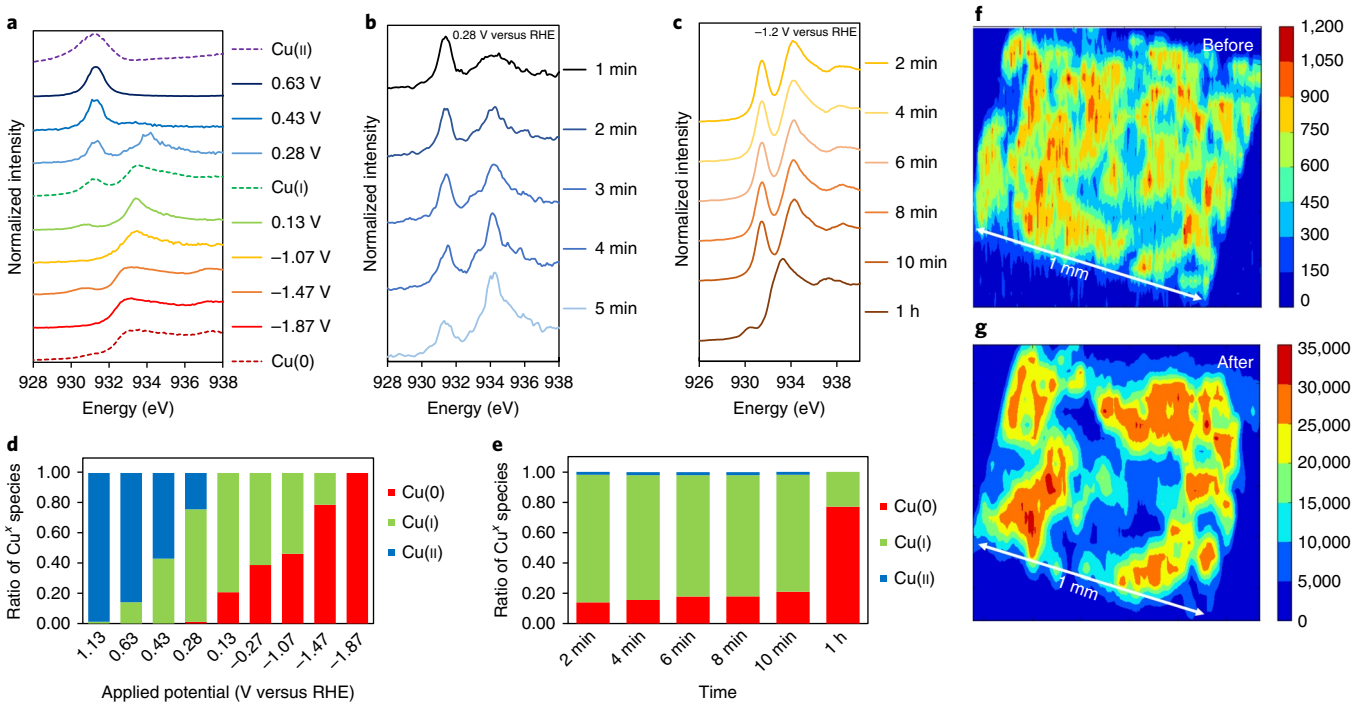

Fig. 4 | X-ray spectroscopy measurements. a, In situ Cu L_3-edge sXAS spectra of ERD Cu at different applied potentials (solid lines) and ex situ sXAS spectra of reference standards Cu metal (red dotted), Cu_2O (green dotted) and CuO (purpled dotted). **b**, Cu L_3-edge spectra with respect to time of ERD Cu under a constant applied potential of 0.28 V versus RHE. **c**, ERD Cu under an applied potential of −1.2 V versus RHE over the course of 1 h. **d**, Calculated ratio of Cu oxidation states from linear combination fitting as a function of applied potential. **e**, Calculated ratio of Cu oxidation states with respect to time during 1 h of reaction at −1.2 V versus RHE. **f**,**g**, sXAS two-dimensional mapping of the Cu intensity with the region of interest set to 940 eV with a width of 100 eV before (**f**) and after (**g**) running CO_2RR.

difficult to distinguish between Cu_2O and metallic Cu (refs [45,46]). These results, taken together with the sXAS measurements, provide evidence for the presence of Cu^+ in ERD Cu during CO_2RR.

Investigating structure–property relationships. To explore further structure–property relationships, we examined the role of morphology and oxidation state in the catalytic performance of ERD Cu.

First, we synthesized a dendritic Cu catalyst via electrodeposition[47] that exhibits a highly porous structure with nanoneedles of high curvature as a control sample representative of a Cu catalyst with sharp morphologies but with no Cu^+ present. SEM images show that the high-curvature morphology of the Cu nanoneedles remained consistent before and after reaction at −1.2 V versus RHE for over an hour (Supplementary Fig. 13a–d). This electrode was synthesized using a copper chloride deposition solution onto carbon paper, using the same Cu precursor as ERD Cu.

We then performed electrocatalytic experiments to determine the CO_2RR activity of the Cu nanoneedle control. Major products for the Cu nanoneedles were hydrogen and formate (Supplementary Fig. 14a). The majority of products were C1; there was no applied potential at which FE_{C2+} exceeded FE_{C1} (Supplementary Fig. 14b). Cu nanoneedles performed considerably worse in ethylene selectivity with a max FE_{C2H4} of only 14%, but retained a relatively low FE_{CH4} of 4% (Supplementary Fig. 14d). Despite the decreased selectivity, the current densities of Cu nanoneedles remained similarly high to ERD Cu (Supplementary Fig. 14c). We propose that the high-curvature morphology is responsible for the enhancement in catalytic rate, leading to increased current densities and high local pH.

To provide mechanistic insights into the selectivity of ERD Cu, we used DFT calculations to explore the production of C_2H_4 versus CH_4. Previous mechanistic studies revealed that the reaction pathways for CH_4 and C_2H_4 differ at the bound CO* intermediate[48–51]. Hydrogenation of bound CO* to form bound COH* leads towards the formation of methane while the dimerization of two bound CO* intermediates leads to the formation of ethylene (Fig. 5a). Another recent study showed that the interface between surface Cu^+ and Cu^0 stabilizes CO–CO dimerization while impeding C1 pathways. This stabilization is due to the electrostatic attraction between oppositely charged carbon atoms induced by the Cu^+ and Cu^0 interface, promoting C–C coupling[52]. We therefore concentrate on the Gibbs free energy of formation for COH* and OCCOH* as descriptors for methane formation and CO–CO dimerization to ethylene[53].

We began by constructing Cu(111) and Cu(211) slabs as model systems of flat and high-curvature Cu surfaces, respectively. To model ERD Cu, we constructed a mixed Cu:Cu_2O slab with 25% Cu^+ species, closely matching the optimal amount of Cu^+ determined from sXAS studies. The ERD Cu(111) and ERD Cu(211) slabs serve as model systems for flat and high-curvature ERD Cu surfaces, respectively[28]. It was found that the Gibbs free energy of formation of the OCCOH* intermediate was lowest (1.13 eV) on the ERD Cu(211) system, 0.76 eV lower than the Cu(211) system, suggesting the presence of Cu^+ is favourable for ethylene production (Fig. 5b). The only surface where the formation of COH* was favoured was on Cu(111). ERD Cu(211) also exhibited the strongest CO binding with a binding energy of −1.45 eV (Fig. 5c and Supplementary Table 6). Interestingly, DFT calculations also suggested that CH_4 is more favourable on ERD Cu than bulk Cu. However, experimentally, we observe severe methane suppression, which suggests that methane suppression cannot be explained fully by thermodynamic effects alone. Rather, methane suppression can be rationalized by the morphology-induced high current densities, which results in high local pH and unfavourable kinetics for CO hydrogenation to COH*. These DFT results suggest that Cu^+ plays a crucial role in stabilizing the OCCOH* intermediate, shifting the

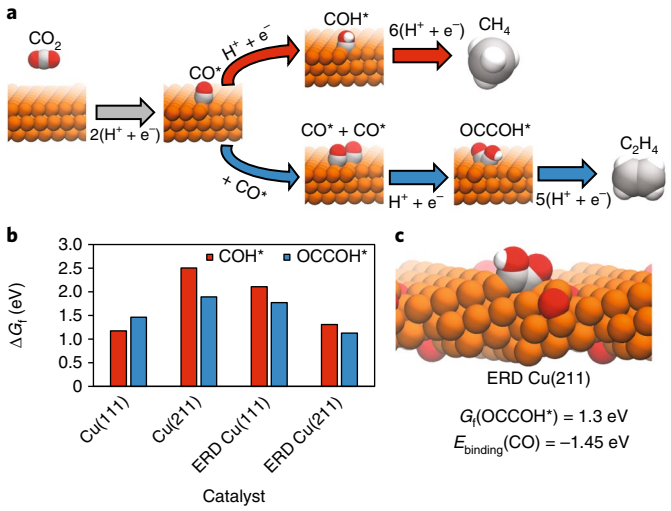

Fig. 5 | DFT studies of C1 and C2 electroproduction as a function of metal oxidation state. a, The reaction mechanisms for the hydrogenation of bound CO to CH_4 (red) and the CO–CO dimerization pathway to C_2H_4 (blue). **b**, The Gibbs free energy of formation of COH* and OCCOH* on Cu(111), Cu(211), ERD Cu(111) and ERD Cu(211) representative of flat Cu, high-curvature Cu, flat ERD Cu and high-curvature ERD Cu respectively. **c**, Optimized structure of bound OCCOH* on ERD Cu at the interface of Cu^+ and Cu^0 species. G_{form}, Gibbs free energy of formation; $E_{binding}$, binding energy.

reaction towards C2 rather than C1 products, and is consistent with experimental observations of ERD Cu.

Discussion

In this study, we present electro-redeposition to realize stabilization of Cu^+ species and optimal morphologies for highly active ethylene production. We found, using in situ sXAS, that the ERD Cu promoted the stability of Cu^+ species at negative potentials far lower than previously reported for up to one hour of reaction. In situ sXAS is experimentally challenging due to the requirement of an ultra-high vacuum environment, and the in situ soft XAS measurements of CO_2 reduction electrocatalysts in this study were enabled only by advanced reaction cells.

We found a catalytic trend where sharper structures with higher-curvature surfaces favour C2+ production. It has been shown previously that sharp tips can improve bubble nucleation, concentrate stabilizing cations and exhibit high local fields, all of which increase current densities[27–30]. This high current density also promotes high local pH, limiting the protonation of bound CO that leads to methane formation[54].

ERD Cu exhibited almost no methane and low carbon monoxide production at the optimal ethylene production potential, highlighting the selectivity of ERD Cu for C2 over C1 gas products. Recent atomistic mechanistic studies have shown that C2 versus C1 selectivity is highly dependent on pH and adsorbed surface water[50,55]. The CO dimerization is the preferred pathway at high pH because hydrogenation of bound CO is kinetically limited. Local pH on the electrode surface is >11 when total current densities reach above 20 mA cm^{-2} due to the rapid consumption of protons[27]. Comparison with Cu nanoneedle controls suggest that the sharp morphology of ERD Cu primarily increases the current density. ERD Cu shows extremely high current densities (60 mA cm^{-2} in H-cell, 450 mA cm^{-2} in flow cell), and consequently a high local pH. Thus, methane suppression is likely enabled by the high local pH provided by ERD Cu. In studies of Cu^+ catalytic enhancement, DFT shows CO binding is stronger on ERD Cu, providing a greater probability of bound CO to interact and dimerize. Simulations also provide evidence that Cu^+ stabilizes the OCCOH* intermediate along the ethylene pathway, favouring the electrosynthesis of C2 products.

In summary, we present ERD Cu as a means to control morphology and oxidation state to suppress methane production and increase ethylene production. We investigated the electronic structure of ERD Cu using in situ sXAS under CO_2RR conditions and varying applied potentials with time resolution to reveal the presence of Cu^+ at highly negative reducing potentials. A correlation between C2+ selectivity, morphology and oxidation state is elucidated whereby sharp features kinetically limit methane formation through local pH effects while the presence of Cu^+ stabilizes ethylene intermediates. The result is an ethylene partial current density of 161 mA cm^{-2} at −1.0 V versus RHE with an ethylene/methane ratio of 200. This study presents electro-redeposition as an unexplored materials strategy to exploit electronic and morphological effects for increased activity and selectivity of CO_2 reduction catalysts.

Methods

DFT calculations. DFT calculations were performed with the Vienna Ab initio Simulation Package (VASP)[56]. Full details are in the Supplementary Information.

Synthesis of ERD Cu and Cu nanoneedle catalysts. The sol–gel precursor was prepared using an epoxide gelation synthesis (further details are in the Supplmentary Information)[34,35]. The active catalyst was then formed by reducing the sol–gel at a specific applied potential in CO_2 saturated 0.1 M $KHCO_3$ electrolyte (pH 7.2). The colour of the catalyst began to change from blue to black within 5 min and was completely black by 10 min regardless of potential applied, resulting in the active ERD Cu catalyst. The Cu nanoneedle catalysts were synthesized following a modified procedure[47]. Cu nanoneedles were electrodeposited on carbon paper from a deposition solution of 0.15 M $CuCl_2$ in 0.5 M HCl using an applied potential of −0.7 V versus Ag/AgCl for 1,000 s.

In situ X-ray absorption. X-ray absorption measurements at the Cu L-edge and K-edge were performed at the spherical grating monochromator beamline 11ID-1 and soft X-ray microcharacterization beamline at the Canadian Light Source. All in situ fluorescence yield mode measurements were performed using a custom flow cell with the catalyst immersed in CO_2 saturated 0.1 M $KHCO_3$ electrolyte at open-circuit potential for at least 30 min before applying a potential. The window of the sample cells was mounted at an angle of roughly 45° with respect to both the incident beam and the detectors. The bodies of the sample cells were fabricated on an SLA NEXT 3D printer. Silicon nitride membrane windows (1 mm × 1 mm × 100 nm) in Si frames (5 mm × 5 mm × 525 μm) were purchased from SPI Supplies. Catalyst ink (20 μL) was drop-casted onto the windows and allowed to dry in air. For electrochemical flow cells, the windows were treated by HF, and then coated by electron-beam evaporated titanium (10 nm) and gold (30 nm), which served as the working electrode. Silver and platinum wires were used as reference and counter electrodes, respectively. The calibration of Ag wire reference electrode was conducted in the standard three-electrode system (the same system as that for performance measurements) as reference electrodes, using Pt foil as working and counter electrodes. The 0.5 M H_2SO_4 electrolyte (pH = 0.3) was pre-purged with Grade 4 H_2 overnight and continuously bubbled with H_2 with a flow rate of 25 ml min^{-1} during calibrations. Linear sweep voltammetry (LSV) was run around ±100 mV between hydrogen evolution and oxidation, and the potential of zero current was recorded. The potential of zero current was around 0.2198 V (including pH correction of 0.3 × 0.0591 = 0.0177 V) for Ag/AgCl electrode and 0.3306 V (including pH correction) for Ag wire electrode, resulting in a calibration of $E_{Ag/AgCl(KCl,\,sat)} + 0.1108\,V = E_{Ag\,wire}$, which is the same as the previous reported value[57]. The windows were then screwed onto the cell forming an air-tight electrolyte chamber of ~1 mm height.

All measurements were made at room temperature in the fluorescence mode using Amptek silicon drift detectors (SDDs) with an energy resolution of approximately 120 eV. Four SDDs were employed simultaneously. The scanning time was 1 min and repeated five times. The sample measurement spot was moved 0.1 mm between measurements at different applied potentials to minimize the effect of the X-ray beam on the sample. The scanning energy range of the Cu L-edge was from 920 to 960 eV. The partial fluorescence yield was extracted from all SDDs by summation of the corresponding Cu L-emission lines.

To determine the concentration of different Cu species, the XAS spectra of Cu standards (Cu, Cu_2O and CuO, representing the 0, 1+ and 2+ oxidation states of Cu, respectively) were measured. Each in situ XAS measurement was then decomposed into a linear combination of these three Cu standards with a simple linear least squares script written in MATLAB. An R^2 value was obtained as a metric for the quality of the fitting. To determine the magnitude of each species'

XAS spectrum, the standards were normalized by matching the pre-edge and post-edge values simultaneously to account for potential changes in the cross-section of the material throughout the measurement. In addition, to account for self-absorption and other measurement artifacts that lead to the appearance of a linear term in the XAS spectrum, a linear term was subtracted from the signal before fitting. Despite all measures taken, it is worth noting that changes in the density of the material could occur, potentially distorting the fitting; however, these effects are considered to be negligible.

X-ray fluorescence mapping was performed on the spherical grating monochromator beamline by rastering the sample across the beam while collecting X-ray fluorescence spectra. The sample is slewed across the beam and the detectors are read out continuously. For the microscopy, the beamspot size was focused to approximately 50 µm using a Kirkpatrick-Baez mirror system.

Characterization. SEM images were acquired using a Quanta FEG 250 or JEOL FE-SEM. TEM images were taken with a Hitachi H-7650 microscope. Dark-field microscopy images were taken with an Olympus BXFM microscope. Powder XRD patterns were obtained with MiniFlex600 instrument. Data were collected in Bragg–Brentano mode using 0.02° divergence with a scan rate of 0.1° s^{-1}. XPS measurements were carried out in a Thermo Scientific K-Alpha system with an Al Kα source with a 400 µm spot size, 50 eV pass energy and energy steps of 0.05 eV. SAM imaging was performed with the PHI 710 Scanning Auger Nanoprobe system, with a cylindrical mirror analyzer and a 25 kV coaxial field emission electron gun.

Electrochemical reduction of CO_2. The CO_2RR activity of the ERD Cu catalysts was investigated by performing electrolysis in a two-compartment H-cell in CO_2 saturated 0.1 M potassium bicarbonate ($KHCO_3$) electrolyte (see the Supplementary Information for details on flow-cell configuration and long-term stability). The three-electrode set-up was connected to a potentiostat (Autolab PGSTAT302N). Ag/AgCl (saturated KCl) was used as the reference electrode and platinum foil was used as the counter electrode. The reaction was performed at constant IR-corrected potential and the products were taken after at least 1 h of continuous run time. Potentiostatic electrochemical impedance spectroscopy with a potential range of −5 to 5 V, 100 kHz frequency and sinus amplitude of 10 mV was used to calculate the IR correction. The resistance values were 34 Ω and 4.5 Ω for H-cell and flow-cell configurations, respectively. Reaction products were quantitatively determined using gas chromatography and nuclear magnetic resonance for gas and liquid products, respectively. Electrode potentials were converted to RHE using the following equation, $E_{RHE} = E_{Ag/AgCl} + 0.197\,V + 0.0591 \times pH$.

The experiments were performed in a gas-tight, two-compartment H-cell separated by an ion exchange membrane (Nafion 117). The electrolyte in the cathodic compartment was stirred at a rate of 300 r.p.m. during electrolysis. CO_2 gas was delivered into the cathodic compartment at a rate of 20.00 sccm and was routed into a gas chromatograph (PerkinElmer Clarus 600). The gas chromatograph was equipped with a Molecular Sieve 5A capillary column and a packed Carboxen-1000 column. Argon (Linde, 99.999%) was used as the carrier gas. The gas chromatography columns led directly to a thermal conductivity detector and a flame ionization detector. The number of moles of gas product were calculated from gas chromatography peak areas with conversion factors for CO, H_2 and ethylene based on calibration with standard samples at 1.013 bar and 300 K. NMR was used to determine the liquid products. ^{1}H NMR spectra were collected on Agilent DD2 500 spectrometer in 10% D_2O using water suppression mode, with DMSO as an internal standard. A 10 s relaxation time between the pulses was used to allow for complete proton relaxation. The Faradaic efficiency (FE) was calculated as follows: $FE = eF \times n/Q = 2F \times n/(I \times t)$, where e is the number of electrons transferred, F is the Faraday constant, Q is the charge, I is the current, t is the running time and n is the total amount of product (in moles).

Data availability. The data that support the findings of this study are available from the corresponding author on reasonable request.

Received: 14 June 2017; Accepted: 24 November 2017;
Published online: 15 January 2018

References

1. Armstrong, R. C. et al. The frontiers of energy. *Nat. Energy* **1**, 15020 (2016).
2. Montoya, J. H. et al. Materials for solar fuels and chemicals. *Nat. Mater.* **16**, 70–81 (2017).
3. Peterson, A. A., Abild-Pedersen, F., Studt, F., Rossmeisl, J. & Nørskov, J. K. How copper catalyzes the electroreduction of carbon dioxide into hydrocarbon fuels. *Energy Environ. Sci.* **3**, 1311 (2010).
4. Kuhl, K. P. et al. New insights into the electrochemical reduction of carbon dioxide on metallic copper surfaces. *Energy Environ. Sci.* **5**, 7050 (2012).
5. Van Miltenburg, A., Zhu, W., Kapteijn, F. & Moulijn, J. A. Adsorptive separation of light olefin/paraffin mixtures. *Chem. Eng. Res. Des.* **84**, 350–354 (2006).
6. Li, C. W. & Kanan, M. W. CO_2 reduction at low overpotential on Cu electrodes resulting from the reduction of thick Cu_2O films. *J. Am. Chem. Soc.* **134**, 7231–7234 (2012).
7. Eilert, A. et al. Subsurface oxygen in oxide-derived copper electrocatalysts for carbon dioxide reduction. *J. Phys. Chem. Lett.* **8**, 285–290 (2017).
8. Verdaguer-Casadevall, A. et al. Probing the active surface sites for CO reduction on oxide-derived copper electrocatalysts. *J. Am. Chem. Soc.* **137**, 9808–9811 (2015).
9. Mistry, H. et al. Highly selective plasma-activated copper catalysts for carbon dioxide reduction to ethylene. *Nat. Commun.* **7**, 12123 (2016).
10. Loiudice, A. et al. Tailoring copper nanocrystals towards C_2 products in electrochemical CO_2 reduction. *Angew. Chem. Int. Ed.* **55**, 5789–5792 (2016).
11. Lee, S., Kim, D. & Lee, J. Electrocatalytic production of C3-C4 compounds by conversion of CO_2 on a chloride-induced bi-phasic Cu_2O-Cu catalyst. *Angew. Chem. Int. Ed.* **54**, 14701–14705 (2015).
12. Chen, C. S. et al. Stable and selective electrochemical reduction of carbon dioxide to ethylene on copper mesocrystals. *Catal. Sci. Technol.* **5**, 161–168 (2015).
13. Kas, R. et al. Electrochemical CO_2 reduction on Cu_2O-derived copper nanoparticles: controlling the catalytic selectivity of hydrocarbons. *Phys. Chem. Chem. Phys.* **16**, 12194 (2014).
14. Handoko, A. D. et al. Mechanistic insights into the selective electroreduction of carbon dioxide to ethylene on Cu_2O-derived copper catalysts. *J. Phys. Chem. C.* **120**, 20058–20067 (2016).
15. Gao, D. et al. Plasma-activated copper nanocube catalysts for efficient carbon dioxide electroreduction to hydrocarbons and alcohols. *ACS Nano* **11**, 4825–4831 (2017).
16. Hori, Y., Takahashi, I., Koga, O. & Hoshi, N. Selective formation of C2 compounds from electrochemical reduction of CO_2 at a series of copper single crystal electrodes. *J. Phys. Chem. B* **106**, 15–17 (2002).
17. Kwon, Y., Lum, Y., Clark, E. L., Ager, J. W. & Bell, A. T. CO_2 electroreduction with enhanced ethylene and ethanol selectivity by nanostructuring polycrystalline copper. *ChemElectroChem* **3**, 1012–1019 (2016).
18. Feng, X., Jiang, K., Fan, S. & Kanan, M. W. Grain-boundary-dependent CO_2 electroreduction activity. *J. Am. Chem. Soc.* **137**, 4606–4609 (2015).
19. Eilert, A., Roberts, F. S., Friebel, D. & Nilsson, A. Formation of copper catalysts for CO_2 reduction with high ethylene/methane product ratio investigated with in situ X-ray absorption spectroscopy. *J. Phys. Chem. Lett.* **7**, 1466–1470 (2016).
20. Li, Y. et al. Structure-sensitive CO_2 electroreduction to hydrocarbons on ultrathin 5-fold twinned copper nanowires. *Nano Lett.* **17**, 1312–1317 (2017).
21. Kim, D., Resasco, J., Yu, Y., Asiri, A. M. & Yang, P. Synergistic geometric and electronic effects for electrochemical reduction of carbon dioxide using gold–copper bimetallic nanoparticles. *Nat. Commun.* **5**, 4948 (2014).
22. Roberts, F. S., Kuhl, K. P. & Nilsson, A. High selectivity for ethylene from carbon dioxide reduction over copper nanocube electrocatalysts. *Angew. Chem. Int. Ed.* **54**, 5179–5182 (2015).
23. Raciti, D., Livi, K. J. & Wang, C. Highly dense Cu nanowires for low-overpotential CO_2 reduction. *Nano Lett.* **15**, 6829–6835 (2015).
24. Mistry, H., Varela, A. S., Kühl, S., Strasser, P. & Cuenya, B. R. Nanostructured electrocatalysts with tunable activity and selectivity. *Nat. Rev. Mater.* **1**, 16009 (2016).
25. Huan, T. N. et al. Porous dendritic copper: an electrocatalyst for highly selective CO_2 reduction to formate in water/ionic liquid electrolyte. *Chem. Sci.* **8**, 742–747 (2017).
26. Reller, C. et al. Selective electroreduction of CO_2 toward ethylene on nano dendritic copper catalysts at high current density. *Adv. Energy Mater.* **7**, 1602114 (2017).
27. Burdyny, T. et al. Nanomorphology-enhanced gas-evolution intensifies CO_2 reduction electrochemistry. *ACS Sustain. Chem. Eng.* **5**, 4031–4040 (2017).
28. Liu, M. et al. Enhanced electrocatalytic CO_2 reduction via field-induced reagent concentration. *Nature* **537**, 382–386 (2016).
29. Klinkova, A. et al. Rational design of dfficient palladium catalysts for electroreduction of carbon dioxide to formate. *ACS Catal.* **6**, 8115–8120 (2016).
30. Saberi Safaei, T. et al. High-density nanosharp microstructures enable efficient CO_2 electroreduction. *Nano Lett.* **16**, 7224–7228 (2016).
31. Zheng, X. et al. Theory-driven design of high-valence metal sites for water oxidation confirmed using in situ soft X-ray absorption. *Nat. Chem.* https://doi.org/10.1038/nchem.2886 (2017).
32. Zheng, X. et al. Sulfur-modulated tin sites enable highly selective electrochemical reduction of CO_2 to formate. *Joule* **1**, 794–805 (2017).
33. Chen, L. D., Urushihara, M., Chan, K. & Nørskov, J. K. Electric field effects in electrochemical CO_2 reduction. *ACS Catal.* **6**, 7133–7139 (2016).
34. Zhang, B. et al. Homogeneously dispersed multimetal oxygen-evolving catalysts. *Science* **352**, 333–337 (2016).
35. Sisk, C. N. & Hope-Weeks, L. J. Copper(II) aerogels via 1,2-epoxide gelation. *J. Mater. Chem.* **18**, 2607 (2008).

36. Ma, S. et al. One-step electrosynthesis of ethylene and ethanol from CO_2 in an alkaline electrolyzer. *J. Power Sources* **301**, 219–228 (2016).
37. Patterson, A. L. The Scherrer formula for X-Ray particle size determination. *Phys. Rev.* **56**, 978–982 (1939).
38. Malcherek, T. et al. Structures of the pseudo-trigonal polymorphs of $Cu_2(OH)_3Cl$. *Acta Crystallogr. Sect. B Struct. Sci.* **65**, 334–341 (2009).
39. Neuburger, M. C. Prazisionsmessung der Gitterkonstante von Cuprooxyd Cu_2O. *Z. Phys.* **67**, 845–850 (1931).
40. Fortes, A. D., Suard, E., Lemée-Cailleau, M.-H., Pickard, C. J. & Needs, R. J. Crystal structure of ammonia monohydrate phase II. *J. Am. Chem. Soc.* **131**, 13508–13515 (2009).
41. Rosen, J. et al. Electrodeposited Zn dendrites with enhanced CO selectivity for electrocatalytic CO_2 reduction. *ACS Catal.* **5**, 4586–4591 (2015).
42. Jiang, P. et al. Experimental and theoretical investigation of the electronic structure of Cu_2O and CuO thin films on Cu(110) using X-ray photoelectron and absorption spectroscopy. *J. Chem. Phys.* **138**, 24704 (2013).
43. Grioni, M. et al. Studies of copper valence states with Cu L_3 X-ray-absorption spectroscopy. *Phys. Rev. B* **39**, 1541–1545 (1989).
44. McIntyre, N. S., Sunder, S., Shoesmith, D. W. & Stanchell, F. W. Chemical information from XPS—applications to the analysis of electrode surfaces. *J. Vac. Sci. Technol.* **18**, 714–721 (1981).
45. Fuggle, J. C., Källne, E., Watson, L. M. & Fabian, D. J. Electronic structure of aluminum and aluminum-noble-metal alloys studied by soft-X-ray and X-ray photoelectron spectroscopies. *Phys. Rev. B* **16**, 750–761 (1977).
46. McIntyre, N. S. & Cook, M. G. X-ray photoelectron studies on some oxides and hydroxides of cobalt, nickel, and copper. *Anal. Chem.* **47**, 2208–2213 (1975).
47. Zhang, X., Wang, G., Liu, X., Wu, H. & Fang, B. Copper dendrites: synthesis, mechanism discussion, and application in determination of L-tyrosine. *Cryst. Growth Des.* **8**, 1430–1434 (2008).
48. Schouten, K. J. P., Kwon, Y., van der Ham, C. J. M., Qin, Z. & Koper, M. T. M. A new mechanism for the selectivity to C1 and C2 species in the electrochemical reduction of carbon dioxide on copper electrodes. *Chem. Sci.* **2**, 1902 (2011).
49. Nie, X., Esopi, M. R., Janik, M. J. & Asthagiri, A. Selectivity of CO_2 reduction on copper electrodes: the role of the kinetics of elementary steps. *Angew. Chem. Int. Ed.* **52**, 2459–2462 (2013).
50. Xiao, H., Cheng, T. & Goddard, W. A. Atomistic mechanisms underlying selectivities in C_1 and C_2 products from electrochemical reduction of CO on Cu(111). *J. Am. Chem. Soc.* **139**, 130–136 (2017).
51. Cheng, T., Xiao, H. & Goddard, W. A. Full atomistic reaction mechanism with kinetics for CO reduction on Cu(100) from ab initio molecular dynamics free-energy calculations at 298 K. *Proc. Natl Acad. Sci. USA* **114**, 1795–1800 (2017).
52. Xiao, H., Goddard, W. A., Cheng, T. & Liu, Y. Cu metal embedded in oxidized matrix catalyst to promote CO_2 activation and CO dimerization for electrochemical reduction of CO_2. *Proc. Natl Acad. Sci. USA* **114**, 6685–6688 (2017).
53. Cheng, T., Xiao, H. & Goddard, W. A. Nature of the active sites for CO reduction on copper nanoparticles; suggestions for optimizing performance. *J. Am. Chem. Soc.* **139**, 11642–11645 (2017).
54. Kortlever, R., Shen, J., Schouten, K. J. P., Calle-Vallejo, F. & Koper, M. T. M. Catalysts and reaction pathways for the electrochemical reduction of carbon dioxide. *J. Phys. Chem. Lett.* **6**, 4073–4082 (2015).
55. Xiao, H., Cheng, T., Goddard, W. A. III. & Sundararaman, R. Mechanistic explanation of the pH dependence and onset potentials for hydrocarbon products from electrochemical reduction of CO on Cu (111). *J. Am. Chem. Soc.* **138**, 483–486 (2016).
56. Hafner, J. Ab-initio simulations of materials using VASP: density-functional theory and beyond. *J. Comput. Chem.* **29**, 2044–2078 (2008).
57. Riskin, M., Basnar, B., Katz, E. & Willner, I. Cyclic control of the surface properties of a monolayer-functionalized electrode by the electrochemical generation of Hg nanoclusters. *Chem. Eur. J.* **12**, 8549–8557 (2006).

Acknowledgements

This work was supported by the Canadian Institute for Advanced Research (CIFAR) Bio-inspired Energy Program, the Ontario Research Fund (ORF-RE-08-034), and the Natural Sciences and Engineering Research Council (NSERC) of Canada. This work was also supported by the Director, Office of Science, Office of Basic Energy Sciences, Chemical Sciences, Geosciences, and Biosciences Division, of the US Department of Energy under contract no. DE-AC02-05CH11231 within the Catalysis Research Program (FWP No. CH030201). The authors thank the Canadian Light Source (CLS) for support in the form of a travel grant. The authors acknowledge Y. Li for valuable scientific discussion and assistance with TEM measurements, A. Kiani for assistance with SEM measurements, Y. Hu and M. Norouzi Banis for assistance with in situ XAS cell set-up, and P. Brodersen from the Ontario Centre for the Characterisation of Advanced Materials (OCCAM) Center for assistance with Auger microscopy measurements. P.D.L thanks the Research Council (NSERC) of Canada for the Canadian Graduate Scholarship — Doctoral award and the Michael Smith Foreign Supplement award. M.B.R. gratefully acknowledges support from the CIFAR Bio-Inspired Solar Energy Program. Computations were performed on the SOSCIP Consortium's Blue Gene/Q computing platform. SOSCIP is funded by the Federal Economic Development Agency of Southern Ontario, the Province of Ontario, IBM Canada Ltd., Ontario Centres of Excellence, Mitacs and 15 Ontario academic member institutions.

Author contributions

P.D.L. synthesized the catalyst, performed DFT calculations, SEM, TEM, XAS and electrochemical experiments, and data analysis, and wrote the manuscript. R.Q.-B. performed XAS, XPS and SAM experiments and data analysis, and edited the manuscript. C.-T.D. performed flow-cell experiments and edited the manuscript. M.B.R. edited the manuscript and guided the design of experiments. O.S.B. performed NMR experiments and analysis. P.T. performed XRD experiments. T.R. supervised and guided XAS experiments. P.Y. and S.O.K. supervised experiments. E.H.S designed the study, edited the manuscript and supervised experiments.

Competing interests

The authors declare no competing financial interests.

Additional information

Supplementary information is available for this paper at https://doi.org/10.1038/s41929-017-0018-9.

Reprints and permissions information is available at www.nature.com/reprints.

Correspondence and requests for materials should be addressed to E.H.S.

Publisher's note: Springer Nature remains neutral with regard to jurisdictional claims in published maps and institutional affiliations.